ELSEVIER

Fusion Engineering and Design 38 (1997) 59–86

Fusion Engineering and Design

Systems analysis in support of the selection of the ARIES-RS design point

Charles G. Bathke *, The ARIES Team

Los Alamos National Laboratory, P.O. Box 1663, Los Alamos, NM 87545, USA

Abstract

Systems analysis has been instrumental in the determination of the ARIES-RS reference design point through the evaluation of design options and the economic optimization of design variables. The ARIES-RS reference design point is described as modeled by the ARIES systems code. Parametric sensitivities about the ARIES-RS reference design point are presented that illustrate the economic impact of various design choices considered within the ARIES-RS design study. © 1997 Elsevier Science S.A.

Keywords: ARIES-RS reference design point; Parametric sensitivities; Systems analysis

1. Introduction

Before starting the conceptual design of an electrical power plant based on a reversed shear (RS) tokamak, systems analysis was used to aid in the definition of the ARIES-RS design point. This analysis determined the values of the plasma minor radius a_p; the plasma aspect ratio A; and the plasma ion temperature T_i, that minimize the cost-of-electricity (COE). Generally, minimum COE producing values for these parameters were then selected for the reference design to meet an 80-mill $kW_e h^{-1}$ minimum requirement established in Ref. [1]. For one variable (i.e. aspect ratio), a non-minimum COE producing value was chosen because of a lack of confidence in some scaling relations away from the reference value. Additionally, systems analysis was used to identify and, where possible, resolve problems associated with the horizontal maintenance scheme and the problem of dispersing part of the plasma heat exhaust outside of the divertor.

The systems analysis reported herein was done using the ARIES systems code (ASC). The ASC evaluates the COE of a potential design point, as defined by ASC input parameters (Table 4). The models used in the ASC are described in Refs. [2,3]. Those models that have been developed specifically for the reverse-shear design (i.e. scalings for normalized-β (β_N) and current-drive efficiency, $\gamma_B = n_e 10^{-20} R_T I_p / P_{CD}$) are presented as needed. All analysis is done for a 1-GW_e power plant with a blanket and shield design that is a refinement of the ARIES-II blanket and shield design [2] and is described in Refs. [4–6]. Following the ARIES-II/IV [2] and PULSAR [3] designs, a level of safety assurance (LSA) rating of LSA = 2 has been assumed, and appropriate cost credits have been taken.

* Corresponding author.

PII S0920-3796(97)00112-9

A brief description of the ARIES-RS reference design point is given is Section 2. The parametric systems analysis for the reference design point is presented in Section 3. A summary of the systems analysis appears in Section 4.

2. Design point reference parameters

A summary list of ASC-generated parameters for the reference design is given in Tables 1–3 with the complete ASC output given in Ref. [6]. The primary rationale for selecting the major design parameters was cost minimization (Section 3) and is summarized below. Preliminary observations indicated that the COE variation within the range $3 \leq A \leq 4$ was not significant. Engineering design issues related to the aspect ratio (e.g. a perceived increase in design complexity and difficulty with decreasing aspect ratio) that are described in Ref. [4] and consistency with earlier ARIES designs [1–3,8,9] fixed the aspect ratio at $A = 4$ for the reference design. The final aspect ratio variation (Fig. 12) shows a linear decrease in the cost of electricity with decreasing aspect ratio, because of the following sequence: a more detailed examination of horizontal maintenance indicated the outboard leg of the TF-coils had to be moved outward further from the vacuum vessel to accommodate maintenance ports, etc, in the vacuum vessel than was anticipated in the ARIES-II/IV [2] and PULSAR [3] designs; outward movement of the outboard TF-coil leg makes the constant-tension TF-coils and the PF-coils, by virtue of their position outside of the TF-coils, larger and more expensive; and the increased cost of the magnets and an unrelated decrease in the shield cost reduce the COE optimum aspect ratio to a lower value. The optimum aspect ratio has not been determined and requires further analysis at lower aspect ratios (i.e. $A < 3.5$). The plasma ion temperature was chosen to be $T_i = 18$ keV to minimize the COE of the reference design. Additionally, the plasma minor radius was chosen to be $a_p = 1.38$ m to minimize the COE, subject to an engineering constraint that the peak field at the TF-coil $B_{TF} \leq 16$ T.

Horizontal maintenance has had a significant impact upon the reference design, which is shown in an elevation view in Fig. 1. The outboard TF-coil leg must be displaced 2.56 m from the back of the vacuum vessel on the outboard to provide the necessary space for single-piece removal of the breeding blanket and structural ring

Table 1
Reverse-shear power-plant physics parameter summary

Parameter	Value
Plasma major toroidal radius, R_T (m)	5.52
Plasma minor radius, a_p (m)	1.38
Plasma vertical elongation:	
k_{95}	1.70
k_x	1.89
Plasma triangularity:	
δ_{95}	0.50
δ_x	0.77
Plasma aspect ratio, $A = R_T/a_p$	4.00
On-axis safety factor, q_0	2.78
Circularized safety factor, q^*	2.37
Plasma-edge safety factor, q	3.50
Troyon coefficient, C_T (Tm MA^{-1})	0.05
Plasma beta, β	0.05
Plasma poloidal beta, β_p	2.29
Stability parameter, $\epsilon\beta_p$	0.57
Peak-to-average density, n_0/n	1.45
Peak-to-average temperature, T_0/T	1.50
Normalized edge density, n_E/n	0.29
Ion temperature, T_i (keV)	18.00
Electron temperature, T_e (keV)	18.72
Ion density, n_i (10^{20} m^{-3})	1.72
Electron density, n_e (10^{20} m^{-3})	2.11
Particle-to-energy confinement time, τ_p/τ_E	1.00
Ion-to-electron energy confinement time, τ_{Ei}/τ_{Ee}	1.00
Lawson parameter, $n_i\tau_E$ (10^{20} s^{-1} m^{-3})	2.40
ITER-89P scaling [7] multiplier, H_{89P}	2.34
On-axis toroidal field, $B_{\phi 0}$ (T)	7.98
Radiation fraction, f_{RAD}	0.18
Plasma current, I_p (MA)	11.32
Bootstrap-current fraction, f_{BC}	0.88
Current-drive power to plasma, P_{CD} (MW)	80.77
Charge period, τ_C (h)	N/A
Ramp/Quench period, τ_R/τ_Q (s)	N/A
Ignition period, τ_I (s)	N/A
Burn period, τ_B (h)	∞
De-ignition period, τ_0 (s)	N/A
Dwell period, τ_B (s)	N/A
Current-drive efficiencies:	
I_{EX}/P_{CD} (mA W^{-1})	16.54
γ_B (10^{20} A W^{-1} m^{-2})	1.63

Table 2
Reverse-shear power-plant engineering parameter summary

Parameter	Value
Field at TF coil, $B_{\phi c}$ (T)	15.80
TF-coil stress (MPa)	621.59
TF-coil current density, j_{TF} (MA m^{-2})	31.04
Magnetic-field energy, W_B (GJ)	85.64
Total specific energy, W_B/M_c (MJ tonne^{-1})	29.91
Fusion power, P_F (GW)	2.17
Neutron power, P_N (GW)	1.73
Average neutron wall loading, I_w (MW m^{-2})	3.96
Peak neutron wall loading, $\hat{I}_w$ (MW m^{-2})	5.68
Neutron fluence life-FW/B, $I_w\tau$ (MW year m^{-2})	15.00
Neutron fluence life-R/M, $I_w\tau$ (MW year m^{-2})	45.00
Average blanket energy multiplication	1.21
Average first-wall heat flux, q_w (MW m^{-2})	0.20
Blanket power density, P_{TH}/V_{BLK} (MW m^{-3})	10.33
Current-drive system efficiency, η_{CD}	0.56
Thermal conversion efficiency, η_{TH}	0.46
Thermal power (GWth):	
Peak, $\hat{P}_{TH}$	2.62
Average, P_{TH}	2.62
Auxiliary site power, P_{AUX} (MW)	48.18
Primary loop pumping power (MW)	12.05
Gross electrical power, P_{ET} (GW$_e$)	1.20
Net electrical power, P_E (GW$_e$)	1.00
Recirculating-power fraction, $\epsilon = 1/Q_E$	0.17
Plasma gain, $Q_p = P_F/P_{CD}$	26.83
Engineering gain, Q_E	5.89
Net plant efficiency, $\eta_p = \eta_{TH}(1-\epsilon)$	0.38
Plant capacity factor, p_f	0.76
Masses (tonne):	
First wall	4.73
Blanket and reflector	580.63
Shield	4235
TF-coils	1856
PF-coils	1007
PF-coil spares	417
Fusion power core	12 256
Mass power density, MPD (kW$_e$ tonne^{-1})	66.70
Level of Safety Assurance, LSA	2

through the access tunnel between adjacent TF-coils. If the outboard leg of a constant tension TF-coil is moved further from the vacuum vessel to accommodate the horizontal maintenance scheme, the PF-coils are displaced by the TF-coil size increase further from the plasma than would a TF-coil that conforms to the vacuum vessel, thereby increasing the PF-coils current and mass. To minimize cost penalties associated with a larger TF-coil (i.e. increased TF- and PF-coil costs), the TF-coil was deformed from the constant-tension shape, as is shown in Fig. 1. Although the TF-coils are supported by a cap, the deformation is limited by the magnitude of the bending stress that can be tolerated across the TF-coil structure.

Table 3
Reverse-shear power-plant economic parameters (1992 $)

Account no.	Account title	Cost (million $)
20.	Land and land rights	10.4
21.	Structures and site facilities	331.0
22.	Reactor plant equipment	1390.1
22.1.1	First wall, blanket, and reflector	74.3
22.1.2	Shield	168.0
22.1.3	Magnets	274.0
22.1.3.1	TF-coils	163.4
22.1.3.3	PF-coils	110.6
22.1.4	Supplemental heating systems	164.2
22.1.5	Primary structure and support	53.4
22.1.6	Reactor vacuum systems	163.5
22.1.7	Power supplies	55.3
22.1.8	Impurity control	13.6
22.1.9	Direct energy conversion system	.0
22.1.10	ECRH breakdown system	4.3
22.1	Reactor equipment	970.7
22.2	Main heat transfer and transport	258.3
23.	Turbine plant equipment	284.4
24.	Electric plant equipment	110.6
25.	Miscellaneous plant equipment	56.2
26.	Special materials	11.1
90.	Total direct cost	2193.8
91.	Construction services and equipment	263.3
92.	Home office engineering and services	114.1
93.	Field office engineering and services	131.6
94.	Owner's costs	405.4
96.	Project contingency	524.5
97.	Interest during construction (IDC)	600.1
98.	Escalation during construction (EDC)	0.
99.	Total capital cost	4232.9
		Constant $
[90]	Unit direct cost, UDC ($ kW$_e^{-1}$)	2193.8
[94]	Unit base cost, UBC ($ kW$_e^{-1}$)	3632.8
[99]	Unit total cost, UTC ($ kW$_e^{-1}$)	4232.9
	Capital return (mill kW$_e^{-1}$)	61.46
[40–47, 51]	O and M (1.4%) (mill kW$_e^{-1}$)	9.16
[50]	Blanket replacement (mill kW$_e^{-1}$)	4.63
	Decommissioning (mill kW$_e^{-1}$)	0.50
[02]	Fuel (mill kW$_e^{-1}$)	0.03
	Cost of electricity, COE (mill kW$_e^{-1}$)	75.79

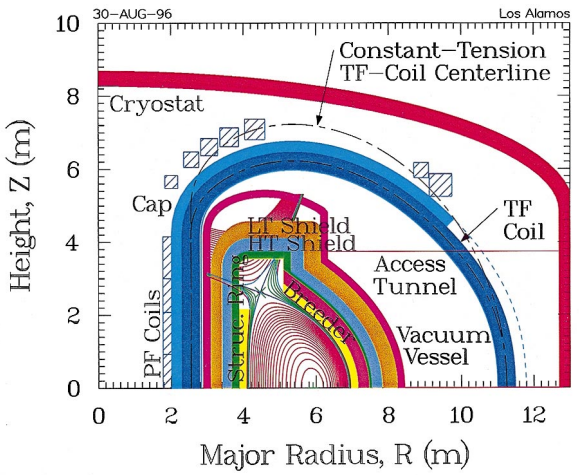

Fig. 1. An elevation view of the ARIES-RS reference design as modeled by the ASC. Shown are the cryostat, the PF- and TF-coils, the cap that supports the coils, the vacuum vessel, the low- and high-temperature (LT and HT) shields, the structural ring that supports the divertor plates and breeding blankets, the access tunnel between the vacuum vessel and the cryostat, and the poloidal flux surfaces. Also shown is the centerline for a constant-tension TF-coil, if one were used.

The thickness of the shield varies poloidally, but is uniform within three poloidal regions. The three shield thicknesses inboard, behind the divertor, and outboard are functions of the neutron wall loading as calculated at three positions on the computational first wall that is shown in Fig. 2: at the inboard equatorial plane, at the top (i.e. where Z is a maximum) of the computational first wall (or directly above the null in Fig. 1), and at the outboard equatorial plane, respectively. The poloidal variation of the neutron wall loading is calculated internal to the ASC and is also displayed in Fig. 2. For the reference design, the neutron wall loadings at the inboard equatorial plane, at the top of the computational first wall, and at the outboard equatorial plane are 3.8, 2.8, and 5.7 MW m^{-2}, respectively; the value for the outboard equatorial plane represents the peak neutron wall loading. The inboard, outboard, and divertor shield thicknesses including gaps for the reference design are 0.56, 0.70, and 0.82 m, respectively. These shield thicknesses reflect the poloidal variation of the neutron wall loading as well as the shielding effects of the blankets. The inboard and outboard blanket thicknesses including gaps are 0.41 and 0.58 m, respectively. Only an 0.2 m thick structural ring is between the plasma and shield in the divertor region. Because there is no breeding blanket to attenuate neutrons in the divertor region, the divertor shield thickness is the largest. Similarly, the inboard shield thickness is determined by the inwardly directed neutron flux between the top of the inboard blanket and the inwardly directed separatrix leg rather than by the flux at the inboard equatorial plane.

The power flow within the power plant is shown schematically in Fig. 3. The plasma current is sustained with 81 MW of current-drive power. The plasma generates a total of 2167 MW of fusion power: 434 MW as charged particles (e.g. αs, protons), 1728 MW in the form of 14 MeV neutrons from DT reactions, and 5 MW of lower-birth-energy (i.e. ≤ 5 MeV) DD and TT neutrons. The energy of the 14 MeV neutrons is multiplied in the blanket and shield by a factor of 1.2, and the energy of the DD and TT neutrons is multiplied by 3.7. The total neutron power available to the thermal cycle for conversion into electricity is 2091 MW. The 515 MW of charged-particle and current-drive power leave the plasma as radiation (91 MW) or transport power (424 MW). Assuming 1% of the transport power is radiated in the SOL before reaching the divertor, then the first wall intercepts 73 MW, 10 MW is lost down various holes in the first wall (e.g. fueling lines, rf ducts), and the remaining 432 MW must be handled by the divertor. However, all of this 515 MW is recovered in the thermal cycle. An additional 12 MW appear in the thermal cycle from the coolant pumps (i.e. pump efficiency) for a total of 2619 MW. At a thermal conversion efficiency of 0.46, 1205 MW of electricity are generated. Of this power 1000 MW are available for selling to customers, 12 MW are needed to drive the coolant pumps, 144 MW are needed to supply the current-drive system, and 48 MW are used for other on-site auxillary power requirements (i.e. lights, etc).

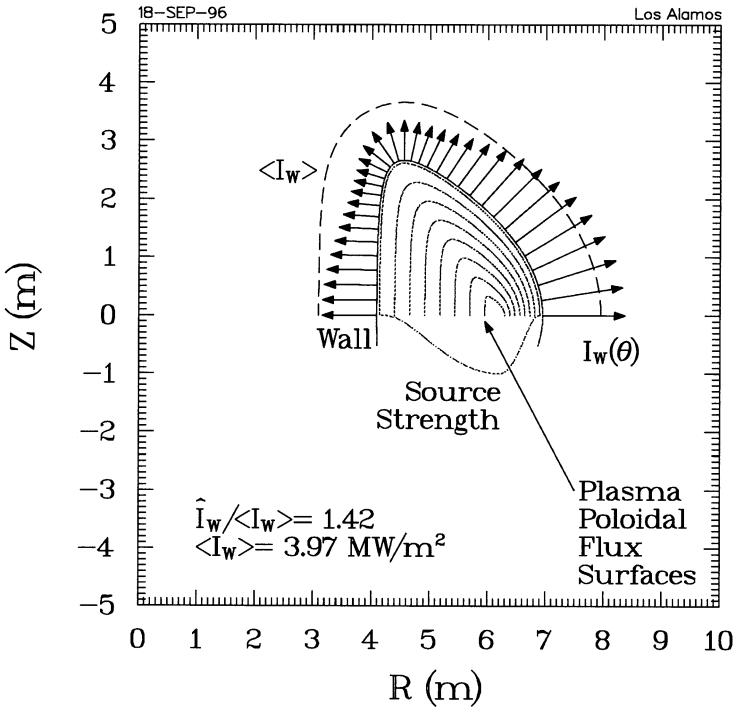

Fig. 2. The poloidal distribution of the neutron wall loading for the ARIES-RS reference design, as modeled by the ASC. Also shown are the plasma closed flux surfaces, the computational wall used for the wall-loading calculation, and the neutron source profile (inverted scale, normalized to −1 at the axis and zero at the plasma edge) in the equatorial plane.

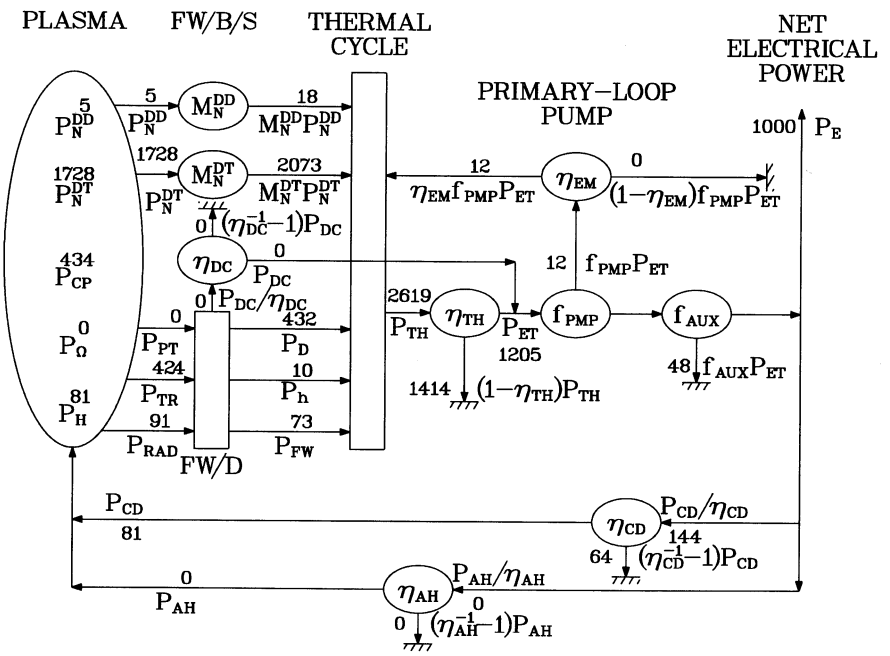

Fig. 3. The plant power flow diagram for the ARIES-RS reference design, as modeled by the ASC.

3. Parametric analysis

The parametric analysis reported herein is limited to the following variables that were considered import during the course of this study: the plasma minor radius, a_p; plasma ion temperature, T_i; plasma aspect ratio, $A = R_T/a_p$; neon impurity fraction, $f_{Ne} = n_N/n_i$; a β scaling factor, f_β, that indicates proximity to the stability limit; TF-coil vertical deformation, δ_v, from a constant-tension shape; the thickness of the outboard gap between the vacuum vessel and TF-coil; number of PF-coil pairs, N_{PF}; PF-coil current density, j_{PF}; and various unit costs that were disputed during the study. Nominal values for the non-economic input variables are given in Table 4. Neither the confinement time nor the magnetic field are input into the ASC. The former is determined by plasma power balance, and the latter is determined by the specified net electrical power, subject to the constraint that the magnetic field at the TF-coil $B_{\phi c} \leq 16$ T. The minor radius is optimized to minimize the cost of electricity in those parametric variations in which the plasma power density is affected; otherwise it is fixed at its nominal value. For information regarding additional parametric sensitivities (e.g. net electrical power or plant factor) the reader is referred to Ref. [2], because the ARIES-II/IV design has a comparable COE and displays similar sensitivities.

Table 4
Fixed quantities for parametric analysis

Parameter	Value
Plasma beta, β (%)	5.0[a]
Circularized safety factory, q^*	2.4
Normalized beta, β_N^{MAX}	4.8
Scale factor, f_β	0.9
Plasma vertical elongation, κ_{95}	1.70
Plasma aspect ratio, $A = R_T/a_p$	4
Plasma minor radius, a_p (m)	1.38[b]
Plasma ion temperature, T_i (keV)	18
Neon impurity fraction, $f_{Ne} = n_N/n_i$ (%)	0.55
TF-coil vertical deformation, δ_v (m)	1.0
Outboard gap between vacuum vessel and TF-coil, δ_0 (m)	2.56[c]
Number of PF-coil pairs, N_{PF}	11
PF-coil current density, j_{PF} (MA m^{-2})	28
Net electrical power, P_E (GW_e)	1
Plant factor, p_f	0.76

[a] The plasma β is calculated from $\beta = f_\beta \beta_N^{MAX}(1+\kappa_{95}^2)/4q^*A$. Scaling relations determined from simultaneously maximizing β, consistent with stability, and bootstrap current are used for β_N^{MAX} and q^* vs. A for fixed κ_{95}. The scale factor f_β is input, and the above nominal value represents a judgement about how close the plasma can be operated to the stability limit without disrupting.

[b] For parametric variations in which the plasma power density is affected, the minor radius is optimized to minimize the cost of electricity, subject to constraints of which the primary constraint is that the magnetic field at the TF-coil $B_{\phi c} \leq 16$ T. For parametric variations in which the plasma power density is unaffected, the minor radius is fixed at the above nominal value.

[c] A clearance between a TF-coil and an extracted blanket sector is the input parameter, which uniquely determines the above value for the outboard gap between vacuum vessel and TF-coil.

3.1. The plasma minor radius

The most basic design parameters pertain to the physical size of the tokamak. Typically, the ASC determines the plasma minor radius that minimizes the COE for a specified plasma aspect ratio and for the other fixed parameters of Table 4 with an internal scan of the minor radius. The COE for such a scan in a_p is shown in Fig. 4 for the ARIES-RS reference design. If unconstrained, the COE displays a minimum in the minor radius resulting primarily from the maximization of the fusion power core (FPC) mass power density (MPD), as shown in Fig. 5; the engineering gain, Q_E, is sufficiently high that recirculating power does not significantly affect the location of the COE optimum in the minor radius. The MPD maximum in the minor radius reflects a balance of magnet costs against other reactor plant equipment costs, as shown in Fig. 6. Three constraints were considered that can restrict the minimum plasma minor radius allowed: (1) the peak field at the TF-coil is constrained to $B_{TF} \leq 16$ T [2]; (2) the peak neutron wall loading is constrained to $\hat{I}_w \leq 10.4$ MW m^{-2} [2]; and (3) no structures comprising the inboard radial build may overlap (i.e. there must be sufficient room on the inboard for blanket, shield, coils, etc). The peak-field constraint is more restrictive than either the wall-loading constraint for ARIES-RS as shown in

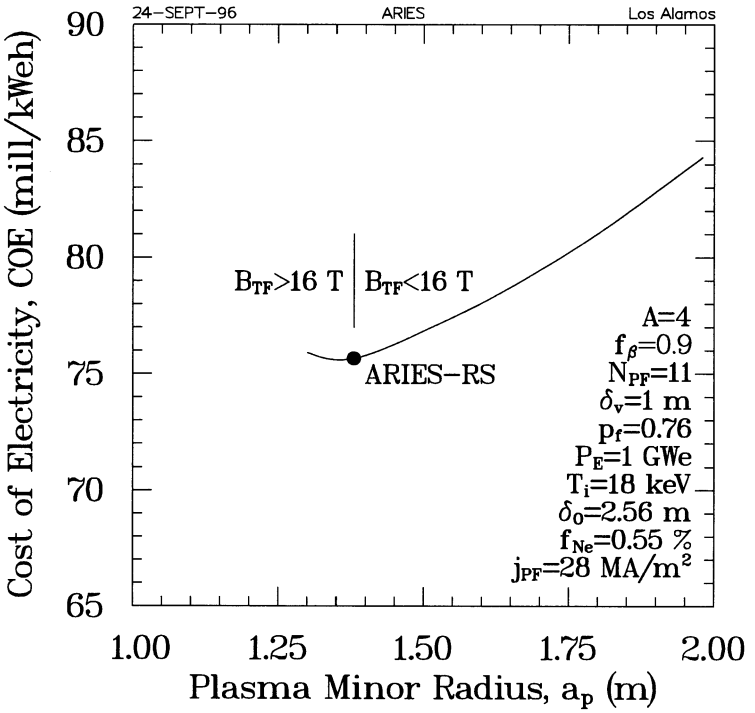

Fig. 4. COE as a function of plasma minor radius calculated internally to the ASC for the fixed parameters of Table 4.

Fig. 5, or the overlap constraint, as shown in Fig. 1.

Both the ARIES-II [2] and ARIES-RS designs use a horizontal maintenance scheme for the blanket. This scheme requires that the outboard leg of the TF-coil be displaced sufficiently far from the vacuum vessel to permit single-piece removal of the breeding blanket horizontally out through adjacent TF-coils. With further development of details of the horizontal maintenance scheme, the thickness of the outboard gap between the vacuum vessel and TF-coils has grown from $\delta_0 =$ 1.77 m for ARIES-II (with a comparably positioned vacuum vessel) to $\delta_0 = 2.56$ m for ARIES-RS. Because the ARIES-RS TF-coil is displaced further from the vacuum vessel, the PF-coils are also displaced further from the plasma and have larger currents and peak fields at the coil than for ARIES-II. The peak field at the PF-coils, B_{PF}, is shown in Fig. 5 for the ARIES-RS reference design. If the peak field at a PF-coil exceeds 8 T, then the superconductor must change from NbTi to Nb_3Sn with a corresponding increase in the coil unit cost. The ARIES-RS reference design has two PF-coils that exceed 8 T (i.e. the peak fields at PF-coils 6 and 7 are 8.86 and 8.17 T, respectively). This problem was recognized too late in the study either to find a PF-coil design below 8 T or to accept a cost penalty for the higher-field PF-coils. One possible solution that is suggested in Fig. 5 is to increase the plasma minor radius to 1.45 m and increase the COE by ~ 0.5 mill kW_eh^{-1}.

A breakdown of the costs of the reactor plant equipment components (i.e. the tokamak plus the heat transfer and transport system) are shown in Fig. 6. The magnet costs increase with decreasing plasma minor radius from the reference design, because the TF-coil current density decreases with increasing field at the coil as the minor radius decreases and the PF-coil currents increase as the PF-coils are moved further from the plasma in a relative sense. The first-wall and blanket, shield, and vacuum-system (i.e. vacuum vessel, cyrostat, pumps, and ducts) costs increase with increasing plasma minor radius because their volumes in-

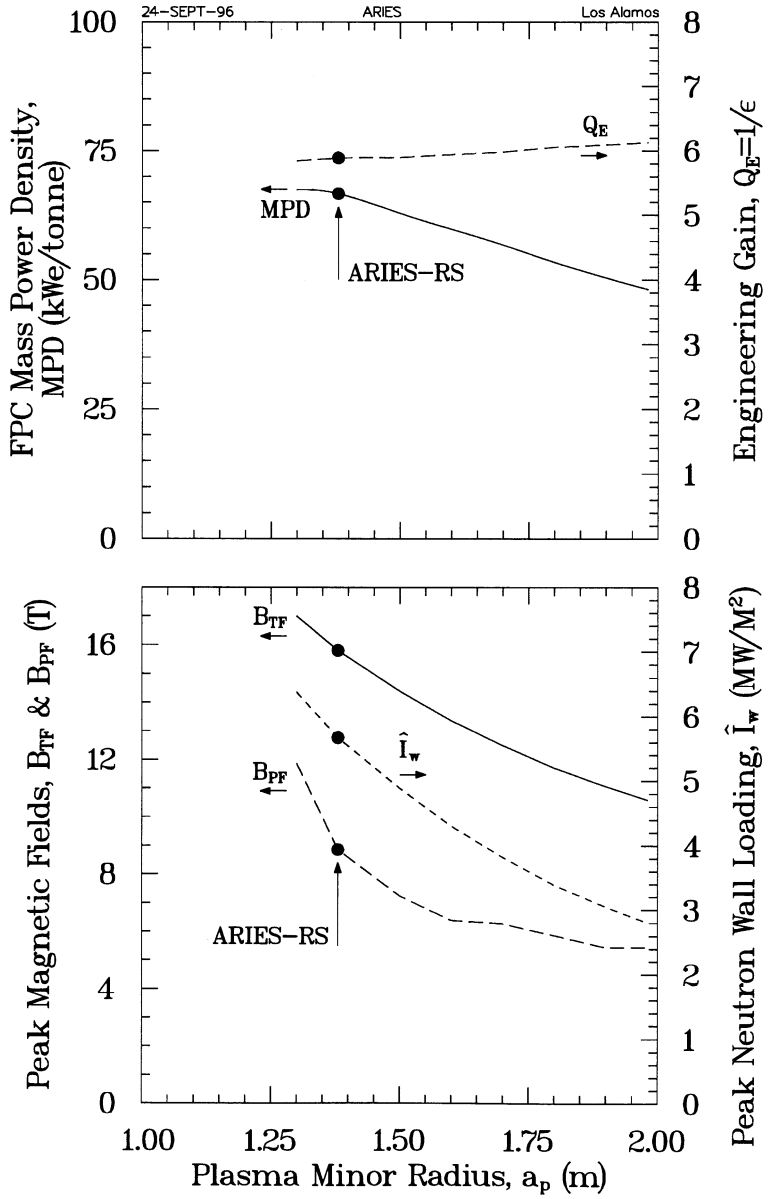

Fig. 5. In the top frame are the mass power density (left scale) and engineering gain (right scale), and in the bottom frame are the peak magnetic fields at the TF- and PF-coils (left scale) and the peak neutron wall loading (right scale) for the minor radius variation of Fig. 4.

crease with increasing plasma minor radius. At a sufficiently large plasma minor radius, the TF-coil current density effect is no longer the dominant effect, and the magnet costs also increase with increasing plasma minor radius because of increasing coil volumes (i.e. conductor length encircling the plasma).

Fig. 6 can also be used to estimate the impact of changing cost upon the location of the COE optimum in the minor radius. Increasing the first-wall and blanket, shield, and/or vacuum-system costs would displace the COE optimum in the

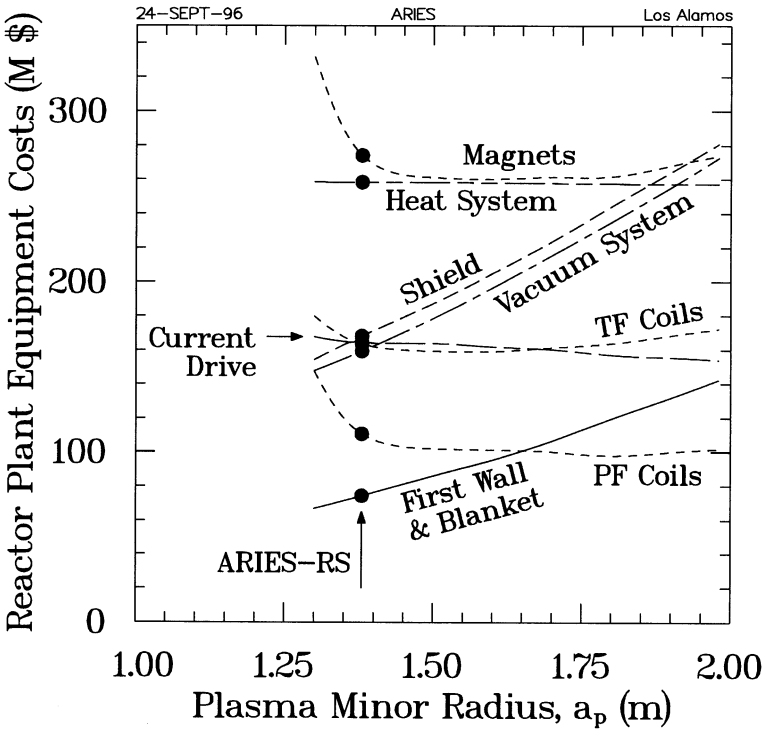

Fig. 6. The major cost components of the reactor plant equipment for the minor radius variation of Fig. 4.

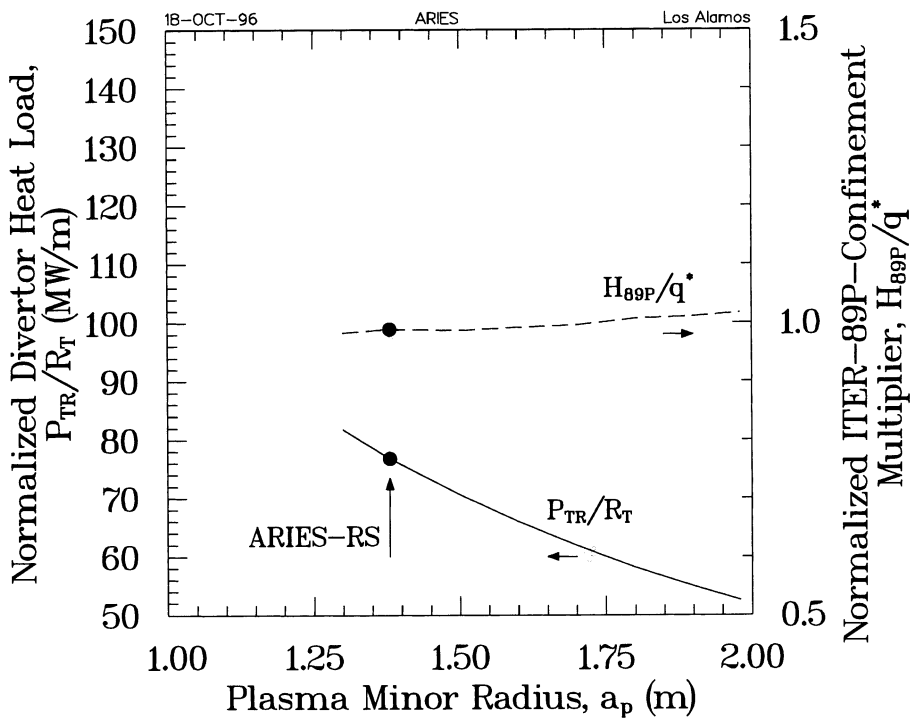

Fig. 7. Physics figures of merit for the divertor heat load (left scale) and energy confinement (right scale) for the minor radius variation of Fig. 4.

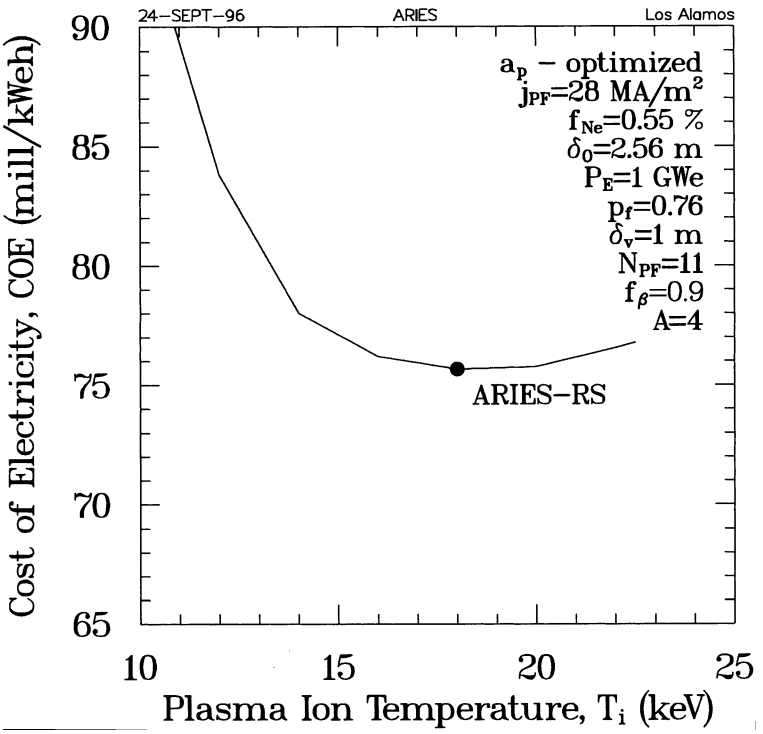

Fig. 8. COE as a function of the plasma ion temperature for the fixed parameters of Table 4. Each point along the curve represents the COE optimum in the plasma minor radius a_p.

minor radius to smaller radius, and increasing the magnet costs would displace the COE optimum to larger radius. However, increasing the magnet costs by 10- or even 100-fold would not increase the COE optimum to minor radii above ≈ 1.45 m, because the region of negative slope in the magnet cost is confined to radii ≤ 1.45 m.

Physics figures of merit are shown in Fig. 7 that characterize the divertor and energy confinement. As expected, decreasing the plasma minor radius increases the normalized divertor heat load, which is defined herein as the transport power, P_{tr}, divided by the plasma major toroidal radius, R_T. The energy confinement figure of merit is defined as H_{89P}/q^*; where H_{89P} is the energy confinement time required for plasma power balance normalized to the energy confinement time predicted by the ITER-89P scaling [7] and q^* is the circularized safety factor. This confinement figure of merit increases only slightly with increasing plasma minor radius and indicates that larger machines need better confinement.

3.2. Plasma ion temperature

The COE sensitivity to variations in the plasma ion temperature is shown in Fig. 8. The COE is strongly dependent upon temperature below 15 keV, but only weakly dependent upon temperature between 15 and 22 keV. At and above 23 keV, the plasma cannot be maintained in power balance against radiation losses, as seen from the plots of the Lawson parameter and radiation fraction in Fig. 9. The temperature that minimizes the COE demonstrates the conflict between simultaneously maximizing the mass power density and the engineering gain, as is shown in Fig. 9. The engineering gain is driven by the current-drive efficiency, which monotonically increases with increasing temperature over the entire temperature range examined (Fig. 9). Increasing engineering gain with increasing temperature decreases the COE and increases the MPD until the engineering gain is no longer the dominant effect (> 14 keV).

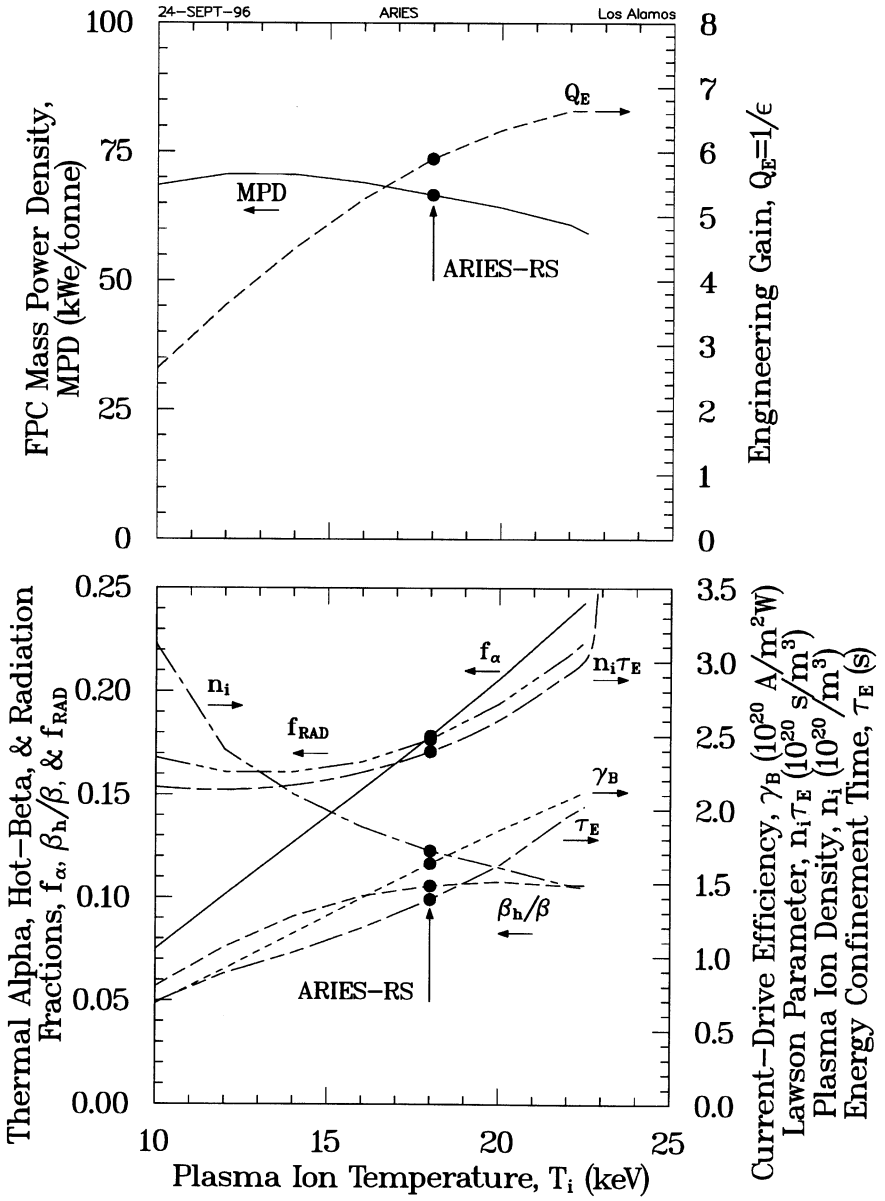

Fig. 9. In the top frame are mass power density (left scale) and engineering gain (right scale), and in the bottom frame are thermal-α density, hot-β, and radiation fractions (left scale) and current-drive efficiency, Lawson parameter, ion density, and energy confinement time (right scale) for the ion-temperature variation of Fig. 8.

The MPD decreases with increasing temperature above 14 keV because of decreased reactivity resulting from fuel dilution. In the higher temperature, lower density plasmas (at constant β), the energy (Fig. 9) and particle ($\tau_p = \tau_E$) confinement times increase with increasing temperature, the ash is better confined, and the ash concentration increases (Fig. 9). A second fuel dilution effect arises because fusion products are thermalized more slowly with increasing plasma temperature (thermalization time is inversely proportional to density) and the hot α-particle pressure increases

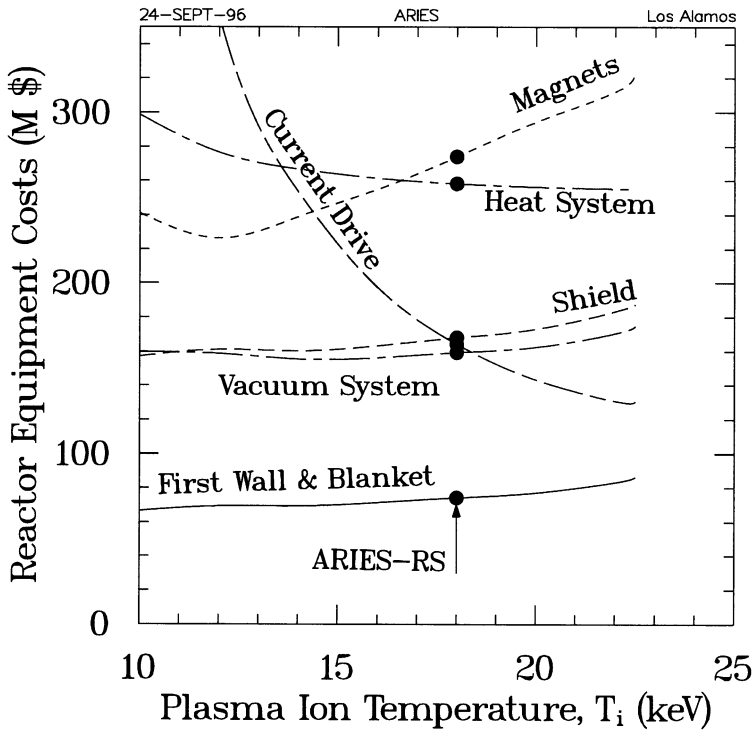

Fig. 10. The major cost components of the reactor plant equipment for the ion temperature variation of Fig. 8.

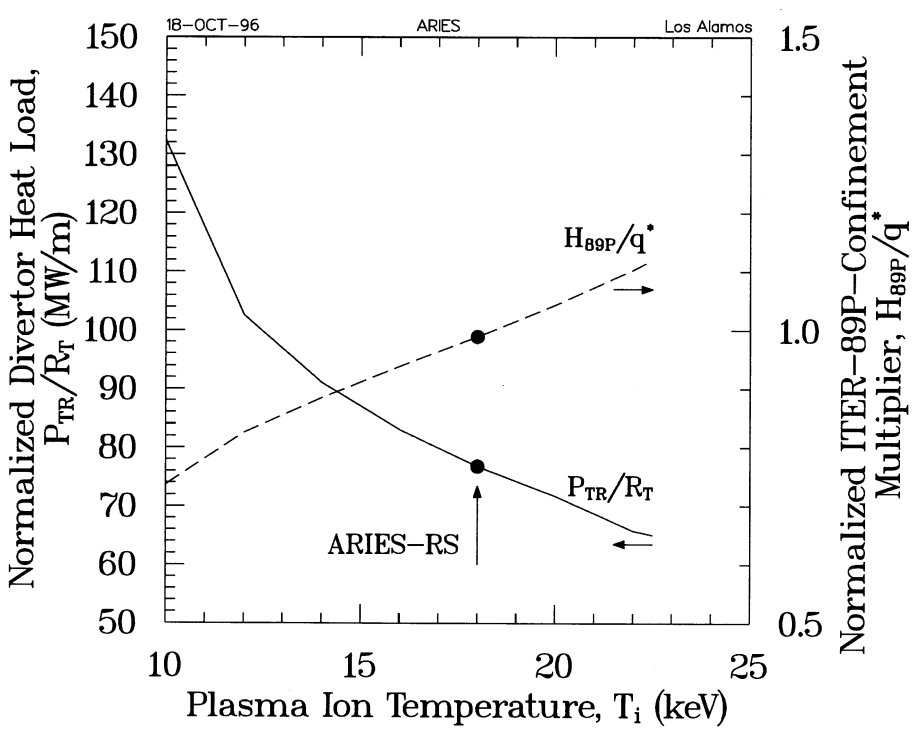

Fig. 11. Physics figures of merit for the divertor heat load (left scale) and energy confinement (right scale) for the ion temperature variation of Fig. 8.

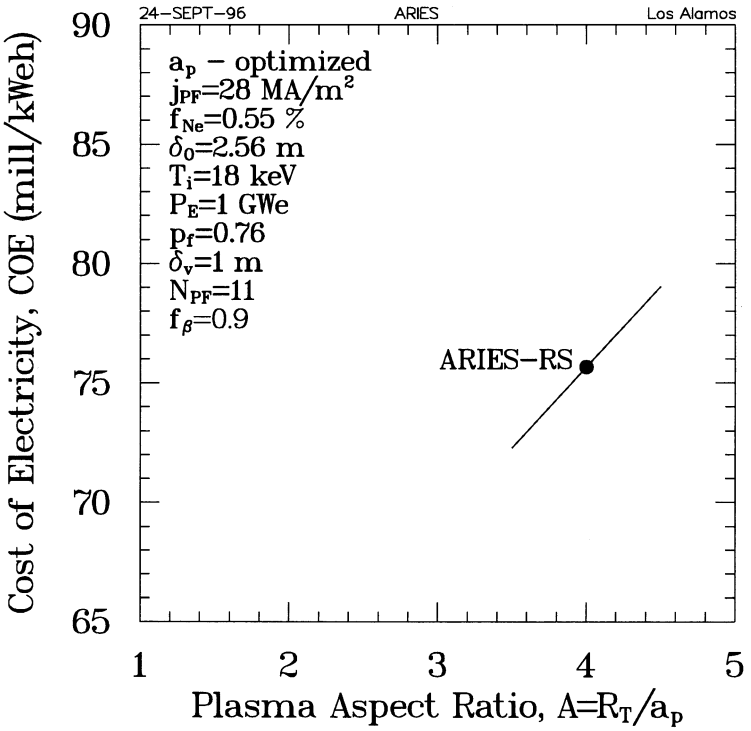

Fig. 12. The cost of electricity as a function of the plasma aspect ratio for the fixed parameters of Table 4. Each point along the curve represents the COE optimum in the plasma minor radius a_p.

(Fig. 9). Both of these fuel dilution effects must be countered with increased toroidal field, which increases TF-coil costs (Fig. 10), to maintain a constant net electrical power.

A breakdown of the costs of the reactor plant equipment components (i.e. the tokamak plus the heat transfer and transport system) is shown in Fig. 10. The current-drive and heat transport (i.e. primary coolant loop, heat exchangers, etc. that are sensitive to recirculating-power levels, because their costs scale as $P_{TH}^{0.55}$; where P_{TH} is the thermal power) systems costs decrease with increasing plasma temperature because current-drive efficiency (i.e. γ_B) increases with increasing plasma temperature. The magnet costs above 12 keV increase with increasing plasma temperature because the machine size must be increased and because the toroidal field must be increased to the maximum allowed by the constraint on the peak field at the TF-coil. Both of the size and field increases are required to compensate for fuel dilution and to maintain a constant net electrical output, as discussed above. The first-wall and blanket, shield, and vacuum-system costs increase slightly with increasing plasma temperature because the plasma volume is also increased to compensate for fuel dilution. The steeper slope of the magnet cost indicates that it is cheaper to increase the toroidal field to the limit permitted by the constraint on the peak field at the TF-coil than to just increase machine size (because the first-wall and blanket, shield, and vacuum-system costs exceed the magnet cost). Increasing current-drive and/or heat-system costs would displace the COE optimum in plasma temperature to a higher temperature; whereas increasing the magnet cost and/or the first-wall and blanket, shield, and/or vacuum-system costs would displace the COE optimum to a lower temperature.

Two physics figures of merit are shown in Fig. 11. The normalized divertor heat load is decreased by a factor of two by increasing the plasma

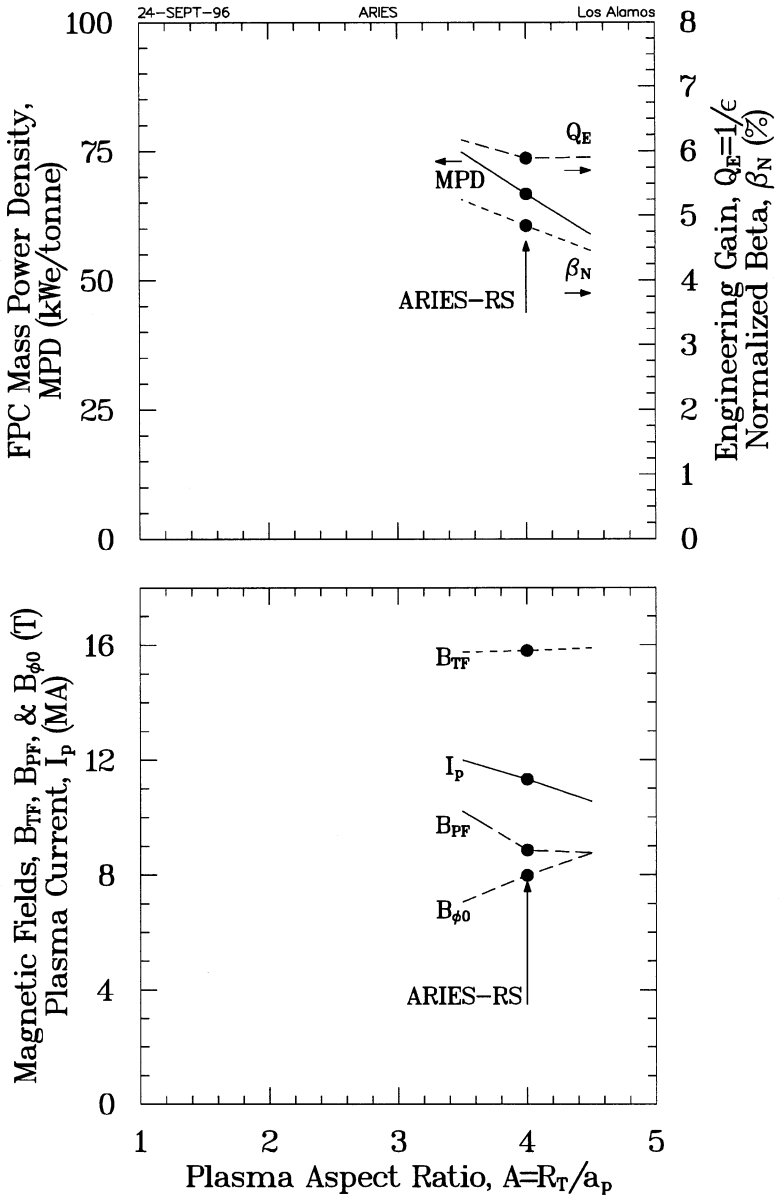

Fig. 13. In the top frame are the mass power density (left scale) and the engineering gain and plasma normalized β (right scale), and in the bottom frame are the plasma current, the peak magnetic fields at the TF- and PF-coils, and on-axis toroidal field for the aspect ratio variation of Fig. 12.

temperature from 10 to 22 keV. This reduction in heat load is the result of an increasing radiation fraction with increasing plasma temperature (Fig. 9). Increasing the plasma temperature (of all the parametric variations studied herein) is the most effective method of reducing the normalized divertor heat load. However, the energy confinement figure of merit increases by a factor of two for the same increase in plasma temperature (i.e. from 10 to 22 keV), implying better confinement is required to operate at higher temperatures.

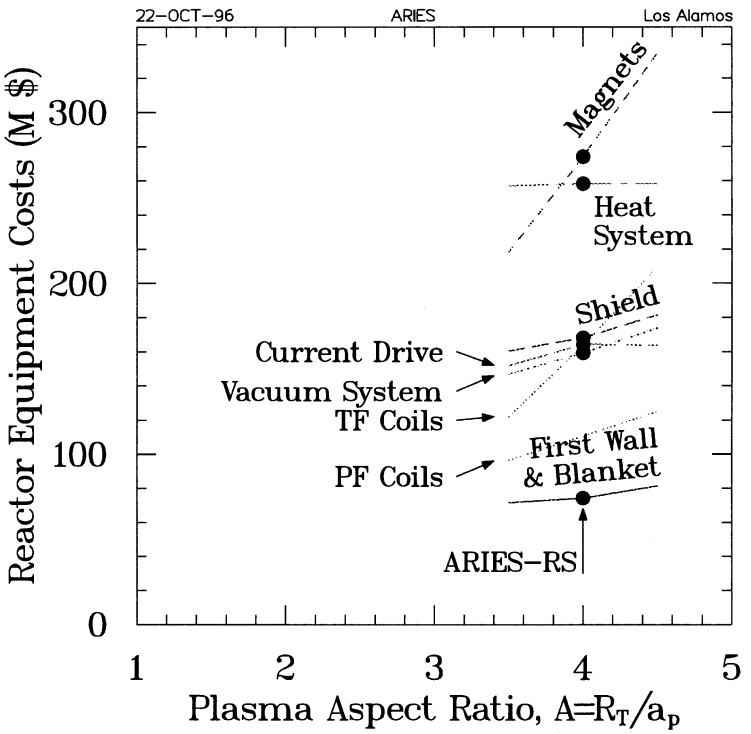

Fig. 14. The major cost components of the reactor plant equipment for the aspect ratio variation of Fig. 12. The magnet cost is comprised of PF- and TF-coil costs, which are also shown.

3.3. Plasma aspect ratio

The dependency of the COE upon plasma aspect ratio is shown in Fig. 12 for reverse shear parameters. The range of aspect ratios investigated has been limited to $3.5 \leq A \leq 4.5$. A detailed current-drive analysis for a non-zero edge density was conducted only at $A = 4$ (see Ref. [10]). Preliminary current-drive analysis for zero edge density indicated that the current-drive efficiency did not vary significantly in the range $3.5 \leq A \leq 4.5$. Consequently, the $A = 4$ current-drive results were extended uniformly over this limited range (i.e. γ_B is assumed independent of A for $3.5 \leq A \leq 4.5$). The ARIES-RS design is the first of the ARIES designs [1–3,8,9] to include the effects of a non-zero edge density in the detailed current-drive analysis. The current-drive efficiency was found to decrease from ≈ 1.75 to $\approx 1.25 \times 10^{20}$ A W^{-1} m^{-2} at $T_i = 14$ keV as a result of including this effect.

The aspect ratio that minimizes the COE occurs at $A < 3.5$. Because the engineering gain is relatively high, as shown in Fig. 13, MPD is the primary discriminating factor in determining the COE dependency upon aspect ratio. The MPD, in turn, is dependent upon the fusion power density (i.e. $\beta^2 B_{\phi 0}^4$). Because β_N increases monotonicly with decreasing aspect ratio, as shown in Fig. 13, the on-axis toroidal field decreases with decreasing aspect ratio, as shown in Fig. 13, to maintain constant net electrical power. Even though the plasma current increases with decreasing aspect ratio, the engineering gain remains approximately constant, because the product of electron density, major toroidal radius, and plasma current is approximately constant (i.e. $\gamma_B = n_e 10^{-20} R_T I_p / P_{CD}$).

The ARIES-II [2] minimum COE occurred at $A \approx 3.2$ and the variation in COE over the range $3.5 \leq A \leq 4.5$ was approximately 2 mill $kW_e h^{-1}$ compared with 7 mill $kW_e h^{-1}$ for ARIES-RS over the same range. This difference between

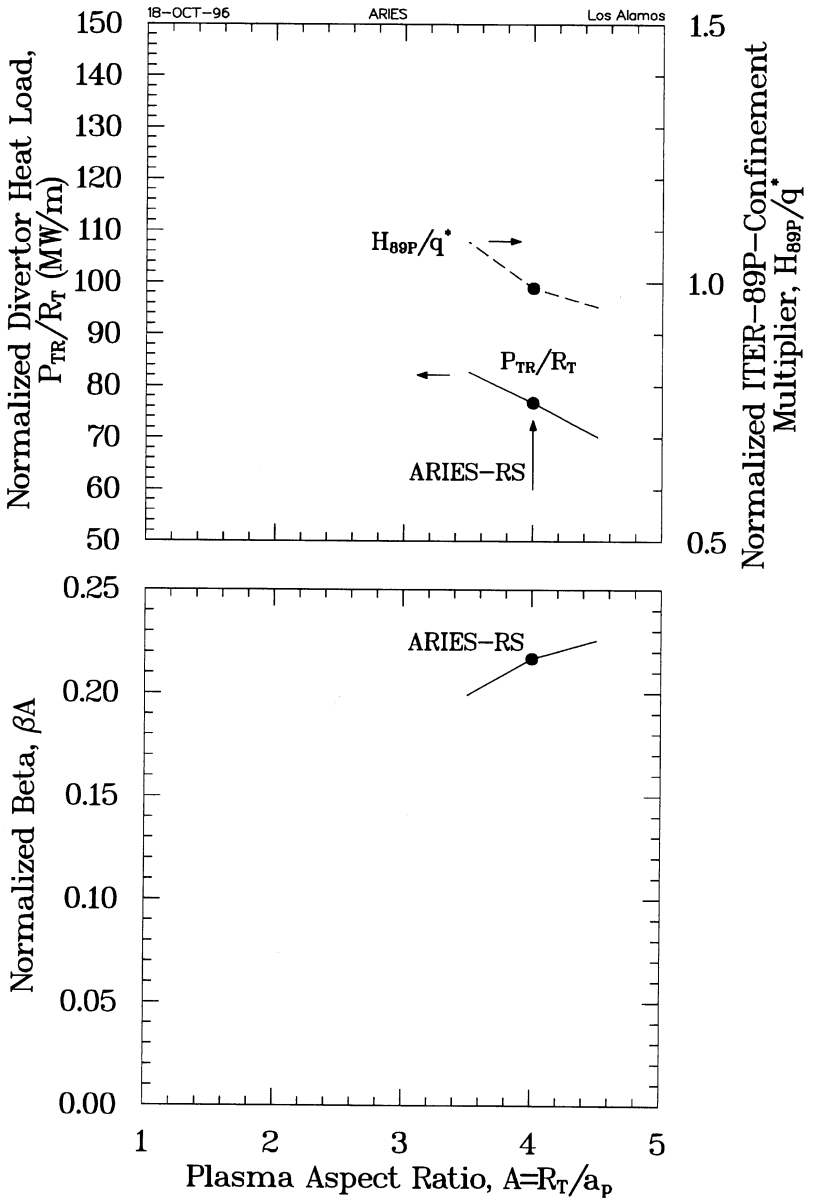

Fig. 15. In the top frome are physics figures of merit for the divertor heat load (left scale) and energy confinement (right scale), and in the bottom frame is the physics figure of merit for β for the aspect ratio variation of Fig. 12.

ARIES-II and ARIES-RS is attributable to the decrease in the cost of the ARIES-RS shield relative to ARIES-II and to an increased magnet cost for ARIES-RS as a result of an increase (dictated by a more detailed examination of the horizontal maintenance scheme) in the thickness of the outboard gap between the vacuum vessel and TF-coils that increases both TF- and PF-coil costs. The two changes in shield and magnet costs displace the COE optimum in aspect ratio to a lower aspect ratio (Fig. 14). The aspect ratio is varied over a larger range that includes the COE

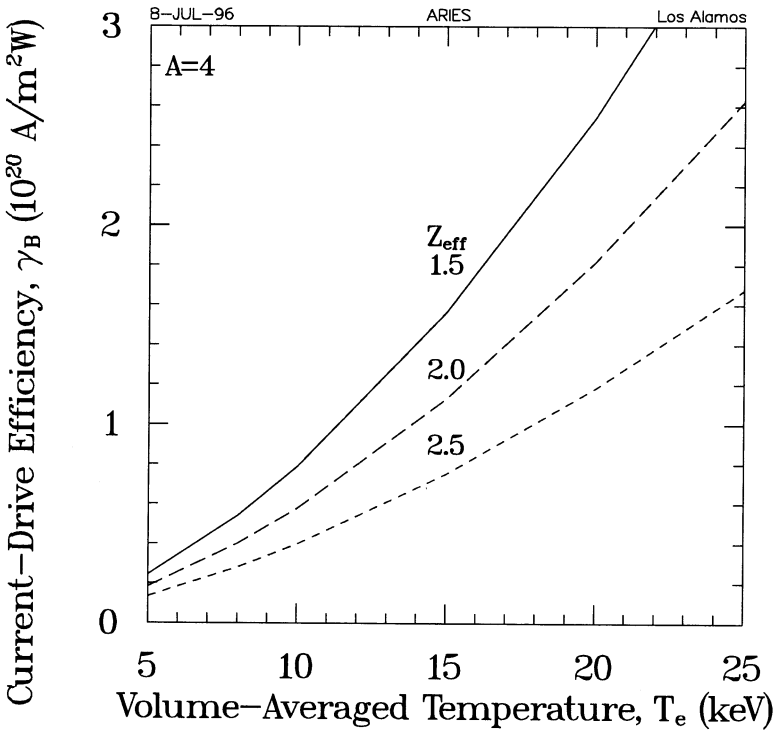

Fig. 16. The current-drive efficiency as a function of the volume-averaged electron temperature for a range of Z_{eff}.

minimum in Ref. [2] than herein, making Figs. 2.3–11 of Ref. [2] more illustrative of the effect of changing system costs on the optimum aspect ratio.

In Fig. 15, increasing the aspect ratio decreases the normalized divertor heat load, because the major radius increases and offers more divertor-plate surface area to receive the transport power. However, the reduction in heat load afforded by increasing the aspect ratio is not as great as that afforded by increasing the plasma temperature (Fig. 11). An additional advantage of increasing the aspect ratio is that the energy confinement figure of merit also decreases. For completeness, the normalized β, βA, is also shown in Fig. 15.

Engineering design issues related to aspect ratio (e.g. a perceived increase in design complexity and difficulty with decreasing aspect ratio) that are described in Ref. [4] and consistency with earlier ARIES designs [1–3,8,9] fixed the aspect ratio at $A = 4$ for the reference design.

3.4. Neon concentration

Throughout the course of this design study several methods to reduce the power to the divertor were studied (Ref. [4,6]). Most of these methods affected only the scrapeoff layer and/or divertor (i.e. not the plasma core), but one method had farther reaching effects. This method was to vary the impurity (i.e. neon) concentration in the plasma core. Preliminary calculations that only considered fuel dilution indicated that doubling the impurity concentration raised the COE only a few mills kW_eh^{-1} and could reduce the transport power by $\approx 25\%$. Further analysis revealed that the impurity concentration in the plasma core has a significant impact on the current-drive efficiency, as shown in Fig. 16. When the effect of impurity concentration upon current-drive efficiency is included, the impurity concentration has a significant impact on the COE, as shown in Fig. 17.

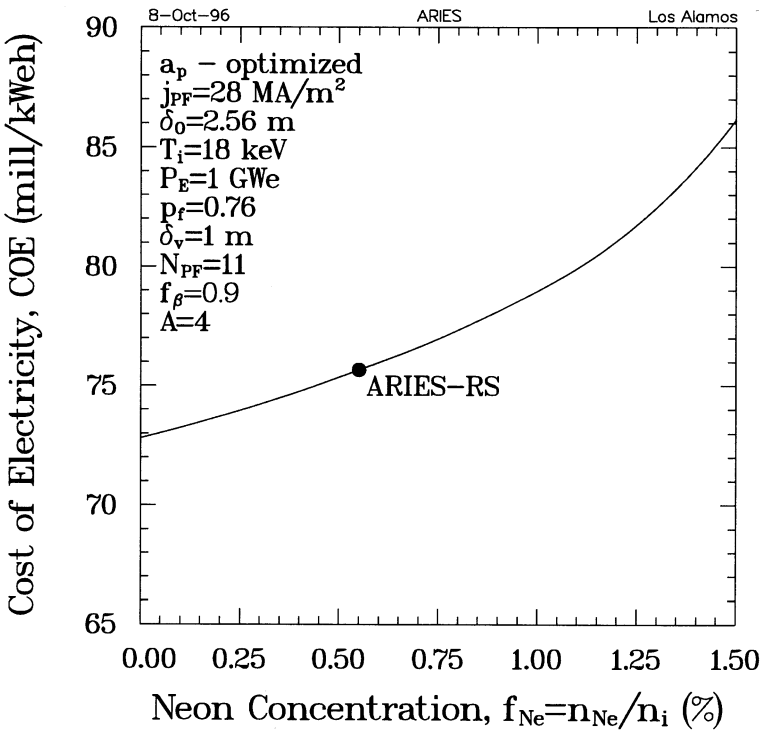

Fig. 17. The cost of electricity as a function of the neon concentration for the fixed parameters of Table 4. Each point along the curve represents the COE optimum in the plasma minor radius a_p.

The neon concentration in Fig. 17 was varied from 0 to 1.5% to affect a variation in plasma charge from $Z_{eff} = 1.3$ to 2.3 and in radiation fraction from $f_{RAD} = 0.13$ to 0.26. The neon concentration for the ARIES-RS design was chosen to yield $Z_{eff} = 1.7$ for consistency with earlier ARIES designs [1–3,8,9]. At a neon concentration of zero, ash is solely responsible for the base $Z_{eff} = 1.3$ and the base radiation fraction $f_{RAD} = 0.13$, as shown in Fig. 18. Such a large variation in the radiation fraction was expected to significantly reduce the transport power entering the scrapeoff layer, and thereby reduce the power that the divertor must handle.

However, the transport power increases with increasing neon concentration because the fusion power must also increase with increasing neon concentration to provide the recirculated power consumed by the current-drive system. The current-drive power deposited in the plasma and the radiation power have negligible effect on transport power, because the powers are comparable and their effects upon the transport power cancel each other out.

The plasma temperature was fixed for the variation of the neon concentration in Fig. 17 to isolate causes and effects. Because increasing the neon concentration significantly decreases the current-drive efficiency, the effect of increasing the neon concentration upon the COE can be mitigated by reoptimizing the plasma temperature. Such a reoptimization would result in the plasma temperature increasing with increasing neon concentration. However, any decrease in either transport power or normalized divertor heat load that would result from increasing the neon concentration with a corresponding increase in plasma temperature would be the result of increasing plasma temperature rather than increasing neon concentration.

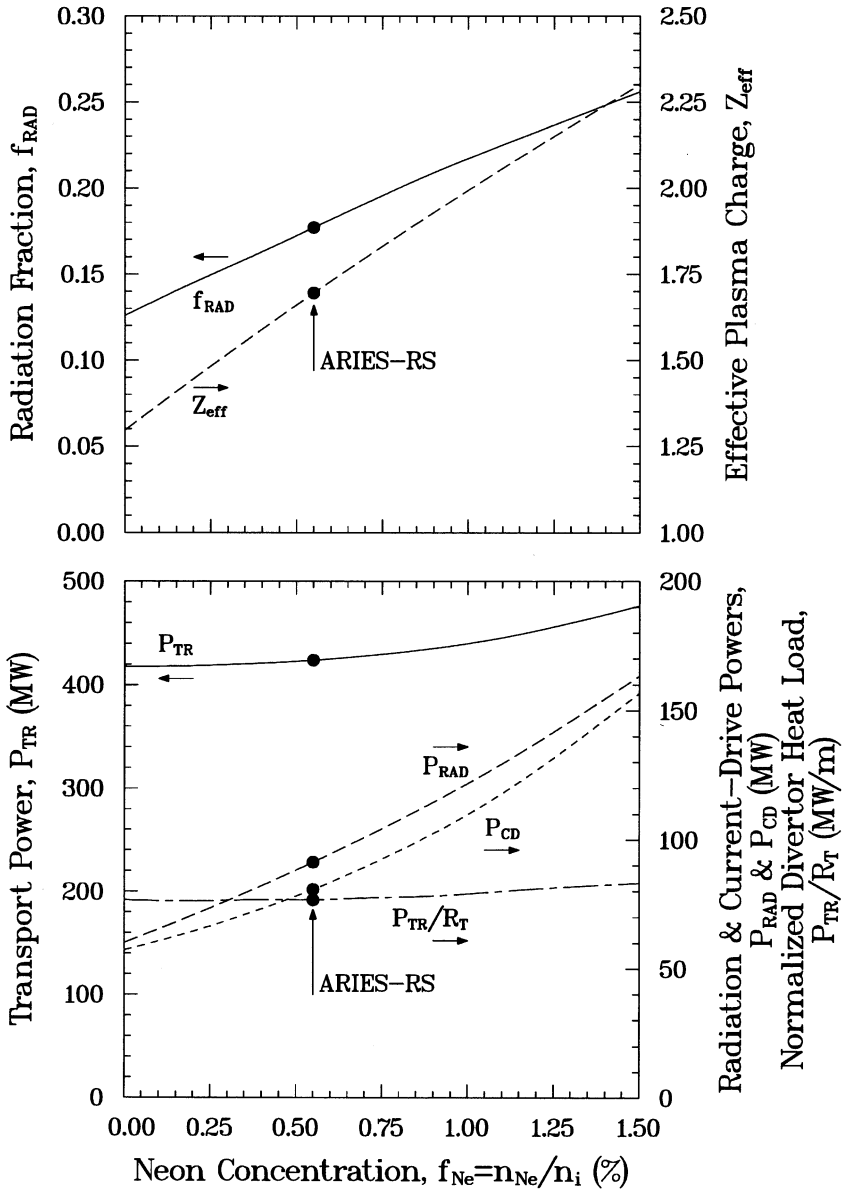

Fig. 18. In the top frame are the core radiation fraction (left scale) and the effective plasma charge (right scale), and in the bottom frame are the transport power (left scale), the radiation and current-drive powers (right scale), and physics figure of merit for the divertor heat load (right scale) for the aspect ratio variation of Fig. 17.

3.5. β

The 5% plasma β of the reference design is below what is typically expected as the maximum β for a reverse shear tokamak. A lesson learned from the previous ARIES designs [2,3,8,9] is that higher bootstrap-current fraction (i.e. lower current-drive power) has a stronger impact on reducing COE than does higher β. Consequently, the β of the reference design results from simultaneously maximizing β, consistent with stability, and meeting the goal of an approximately unitary

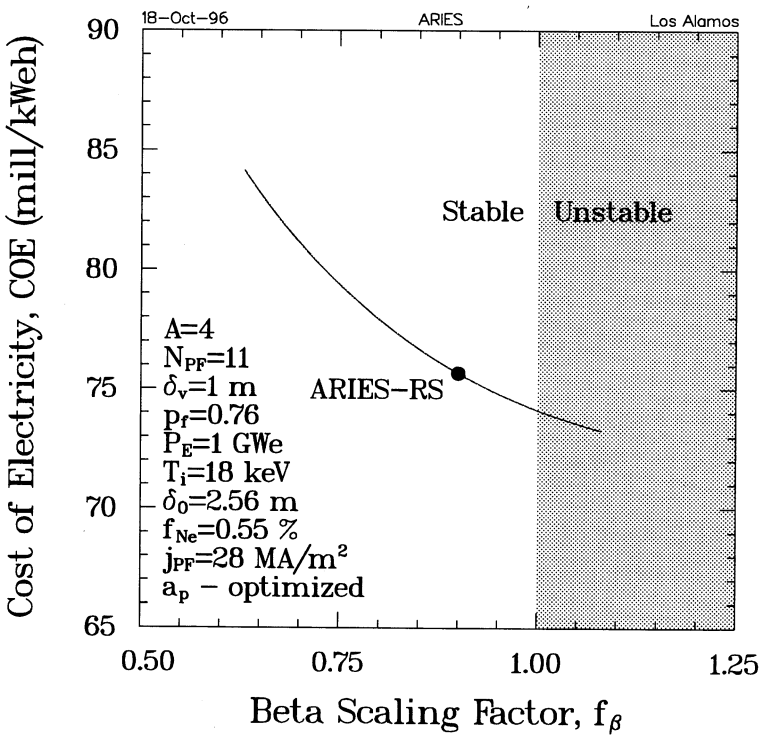

Fig. 19. COE as a function of the β scaling factor for the fixed parameters of Table 4. Each point along the curve represents the COE optimum in the plasma minor radius a_p. The region of MHD unstable equilibria (i.e. $f_\beta > 1$) is also shown.

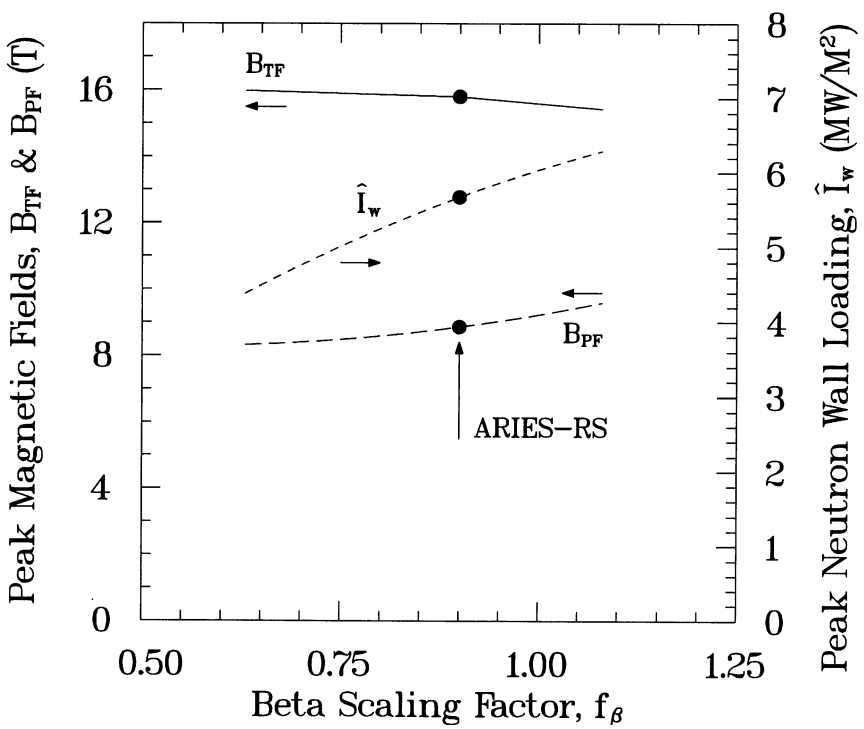

Fig. 20. The peak magnetic fields at the TF- and PF-coil (left scale) and the peak neutron wall loading (right scale) for the β-scaling-factor variation of Fig. 19.

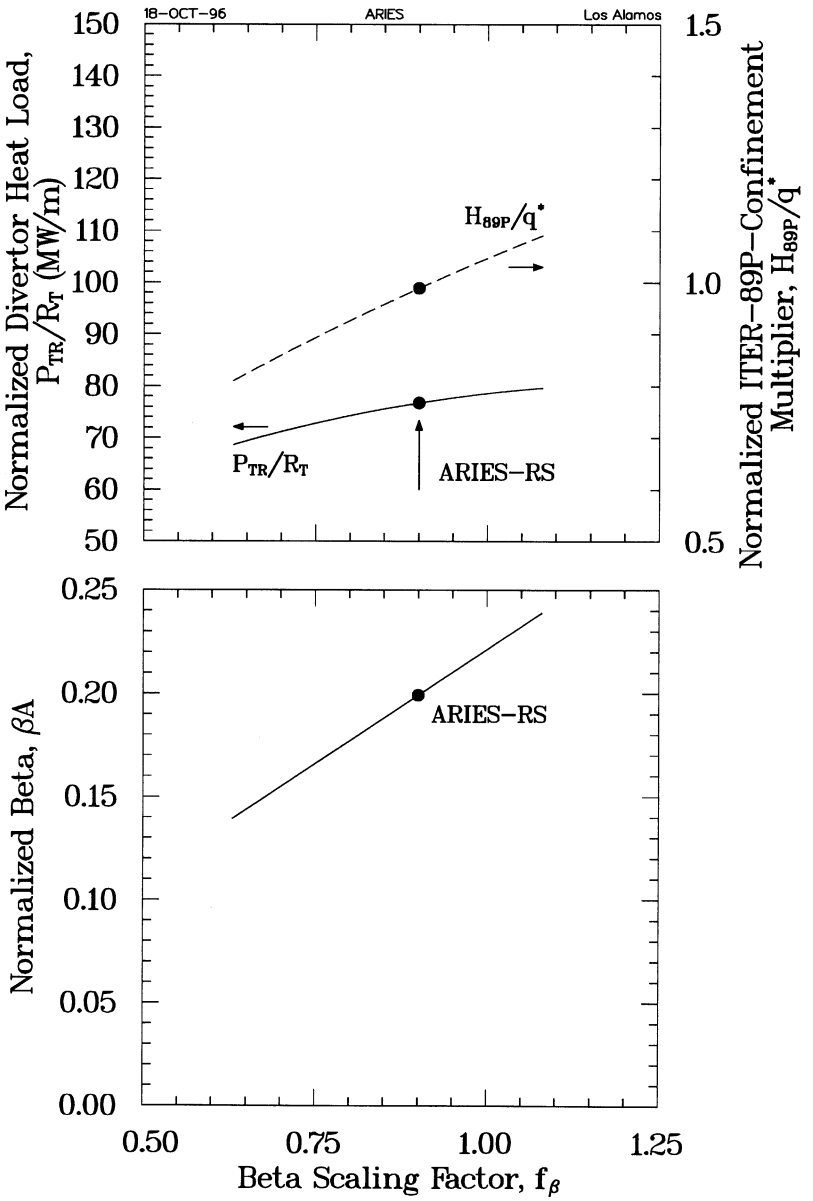

Fig. 21. In the top frame are physics figures of merit for the divertor heat load (left scale) and energy confinement (right scale), and in the bottom frame is the physics figure of merit for β for the beta-scaling-factor variation of Fig. 19.

bootstrap-current fraction (Ref. [10]). To operate at higher β (e.g. 10%) would significantly lower the bootstrap-current fraction, increase the current-drive and recirculated powers, and increase the COE. The variation of β reported herein does not reexamine this tradeoff between β and bootstrap-current fraction, but rather focuses on the issue of the cost associated with having a β safety margin to eliminate plasma disruptions.

To attain a high plant availability, the number of plasma disruptions must not exceed more than one per year (Refs. [1,10,11]). Such a low disrup-

tion rate is affected herein by scaling back the β from the stability limit. A 10% safety margin (i.e. $f_\beta = 0.9$) is adopted herein (Ref. [10]). A sensitivity of COE to the β scaling factor at constant plant availability is provided in Fig. 19; an accurate estimate of the cost of such a safety margin requires a correlation of plant availability with the β scaling factor (i.e. disruption frequency) be included in the analysis. The 10% safety margin increases the COE by ≈ 1.5 mill $kW_e h^{-1}$, which is a reasonable price to pay for the virtual elimination of disruptions.

Increasing the safety margin (i.e. decreasing f_β) decreases the peak neutron wall loading, as shown in Fig. 20. The reduction in wall loading decreases the mass power density that, in turn, increases the COE. The peak field at the PF-coils also decreases, but only slightly, with increasing safety margin, because the reduced mass power density requires a larger plasma minor radius that ultimately moves the PF-coils relatively closer to the plasma (see Section 3.1). Increasing the safety margin decreases the energy confinement figure of merit significantly, as shown in Fig. 21. The normalized divertor heat load is also decreased with increasing safety margin, but to a lesser extent than the energy confinement. For completeness, the normalized beta, βA, is also shown in Fig. 21.

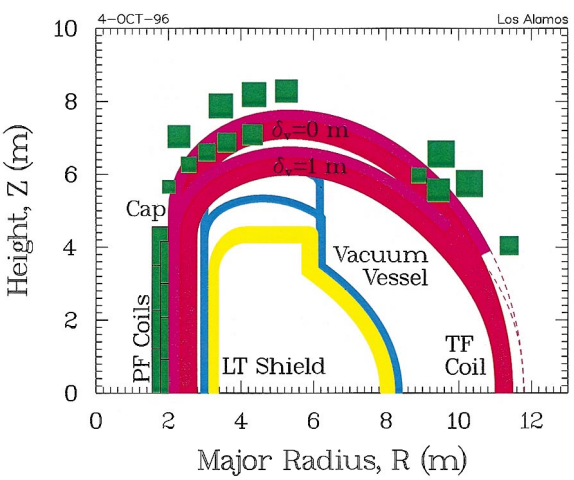

Fig. 22. An elevation view of two design extremes used for the variation of the vertical deformation, δ_v, from a constant-tension TF-coil as modeled in the ASC. Shown are the PF- and TF-coils, the cap that supports the coils, the vacuum vessel, and the low-temperature (LT) shield.

3.6. TF-coil shape

As has been previously mentioned, the deleterious effect of the increased spatial requirement of the horizontal maintenance scheme relative to previous ARIES designs [1–3,8,9] upon the TF- and PF-coils was a major focus of this study. This effect is best illustrated by an inverse unraveling of the TF-coil alterations. The initial response to the increased spatial requirement was simply to increase the size of the constant-tension TF-coil. Increasing the TF-coil size resulted in a cost of electricity that exceeded the 80 mill $kW_e h^{-1}$ minimum requirement established in Ref. [1]. One way to reduce the COE is to deform the TF-coil from a constant-tension shape, as is shown in Fig. 22. As can be seen from Fig. 23, eliminating the vertical deformation (i.e. $\delta_v = 0$) increases the COE by approximately 5 mill $kW_e h^{-1}$. This increase in COE is the result of larger TF- and PF-coils that can be seen qualitatively from Fig. 22; the PF-coils are larger because they are more distant from the plasma and require larger currents to produce the same effect at the plasma for fixed PF-coil current density of 28 MA m^{-2}. Although the initial motivation for vertically deforming the TF-coils was to reduce the COE, a major benefit was to reduce the peak field at the PF-coils, as also shown in Fig. 23. The vertical deformation is limited to ≈ 1 m by the magnitude of the bending stress that can be tolerated across the TF-coil structure [12].

3.7. Outboard TF-coil leg placement

The initial response to the increased spatial requirement of the horizontal maintenance scheme was simply to increase the size of the constant-tension TF-coil. This size increase was accomplished by increasing the displacement of the outboard TF-coil leg from the vacuum vessel, as shown in Fig. 24. The minimum displacement is set by the machine height and is $\delta_0 = 0.61$ m.

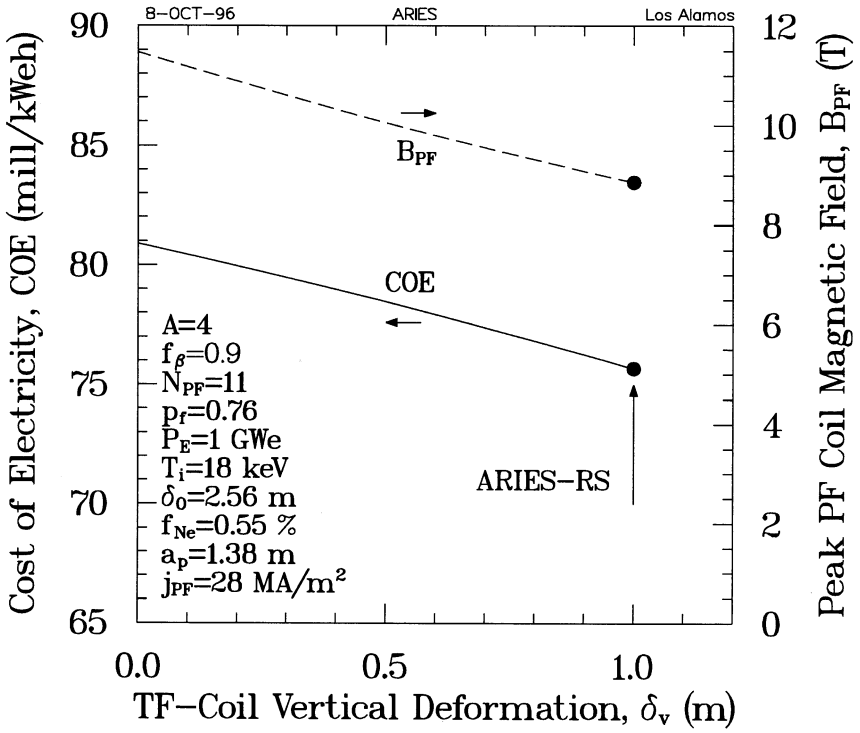

Fig. 23. The cost of electricity (left scale) and the peak field at the PF-coils (right scale) and a function of the vertical deformation from a constant-tension TF-coil (Fig. 22) for the fixed parameters of Table 4.

The design with the snuggest fitting constant-tension TF-coil has a COE of 72.5 mill kW_eh^{-1}, as is indicated in Fig. 25, and would have a PF-coil peak field of 7.3 T, as also seen from Fig. 25. Then the cost penalty of horizontal maintenance using vertically deformed TF-coils is approximately 3 mill kW_eh^{-1} relative to an unspecified maintenance scheme that permits snug fitting constant-tension TF-coils, and the cost penalty using constant-tension TF-coils would be approximately 8 mill kW_eh^{-1}.

3.8. Number of PF-coils

The number of PF-coils was also varied late in the design in an attempt to reduce the PF-coil peak field without affecting any other aspect of the design. Varying the number of PF-coils has no significant impact on th COE, as shown in Fig. 26. Increasing the number of PF-coils decreases the PF-coil peak field slightly. Increasing the number of PF-coils effectively moves the PF-coil current centers closer to the plasma and, thereby, reduces the current and peak field.

3.9. PF-coil current density

A common technique to reduce the field at a PF-coil is to decrease its current density. Lowering the current density moves the coil surface further from the current center and reduces the field at the surface, if the current remains constant. As shown in Fig. 27, the peak field and COE increase as the current density is decreased. As the current density decreases, the PF-coil current centers move away from the plasma, the current increases, and the peak field must also increase ($B_{PF} \approx I_{PF}/r_{PF}$ and $r_{PF}^2 = I_{PF}/j_{PF}$, therefore $B_{PF} \approx \sqrt{j_{PF} I_{PF}}$).

3.10. Unit costs

Projection of unit costs are still uncertain, warranting a sensitivity analyses to the major cost drivers of the ARIES-RS design. From Table 2, the major (≥ 100 M$) cost components of the reactor equipment account are: the shield, magnets, current-drive/heating systems, and vacuum systems (i.e. vacuum vessel, cyrostat, pumps, and ducts). The cost components of the shield and vacuum system that were most debated within the ARIES project are the unit costs of vanadium (only in the first wall, blanket, and high-temperature shield) and of the structural steel (in the low-temperature shield, vacuum vessel, and cyrostat). The reference unit costs for those items are given in Table 5. The change in the cost of electricity that results from the change in a single unit cost is shown in Fig. 28; changes in multiple unit costs would have an accumulative effect on the COE. Changes in the unit costs of the magnets and of vanadium have the greatest effect upon the cost of electricity, because the magnets and vanadium are the two largest cost elements in the reactor equipment. A doubling of either of these unit costs would increase the cost of electricity by 7–8 mill kW_eh^{-1}. The effect of changing the unit cost of the structural steel and of the current-drive/heating systems upon the cost of electricity is half that produced by the magnets and vanadium, because the structural steel and current drive contribute half as much to the total cost of the reactor equipment. The structural steel is twice as prevalent throughout the reactor equipment as vanadium, but the unit cost of structural steel is less than a quarter of that for vanadium.

Varying the unit cost of the current-drive system is significantly different from varying the required current-drive power (i.e. the current-drive efficiency). Varying the current-drive power directly affects the cost of the current-drive system and indirectly affects the cost of everything else, because current-drive power is recirculated power (Fig. 3). The current-drive efficiency is the result of detailed calculations that include temperature and plasma-charge effects. To properly change the current-drive efficiency requires that the temperature and/or plasma charge be changed. The reader is referred to Section 3.2 and Section 3.4 for self-consistent changes in current-drive efficiency.

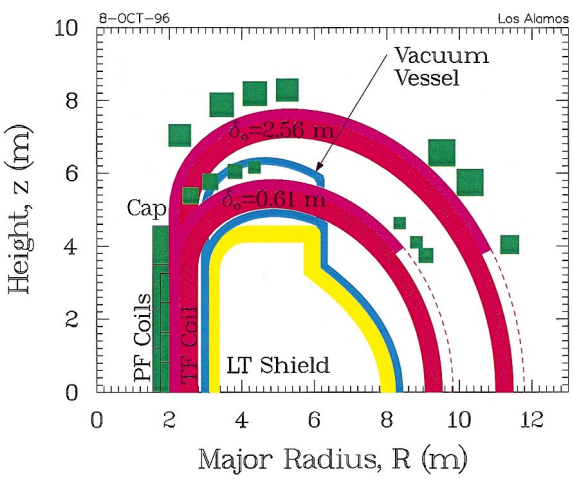

Fig. 24. An elevation view of two design extremes used for the variation of the gap thickness, δ_0, between the vacuum vessel and the TF-coil as modeled in the ASC. Shown are the PF- and TF-coils, the cap that supports the coils, the vacuum vessel, and the low-temperature (LT) shield.

4. Summary

Three significant changes have been introduced in the ARIES-RS design that are absent from earlier ARIES designs (i.e. Starlite [1], PULSAR [3], ARIES-II/IV [2], etc.): the inclusion of a non-zero edge density in the detailed current-drive calculations (Ref. [10]), an increased gap thickness between the vacuum vessel and TF-coil resulting from increased fidelity in the horizontal maintenance model, and deviation from a constant-tension TF-coil. The first two changes add approximately 4 and 5 mill kW_eh^{-1} to the cost of electricity, respectively, and the latter change decreases the cost of electricity by approximately 5 mill kW_eh^{-1} for a net increase in the cost of electricity of approximately 4 mill kW_eh^{-1} from just these three changes. Many other minor model refinements combined to increase the cost of electricity by approximately 2 mill kW_eh^{-1} for a net

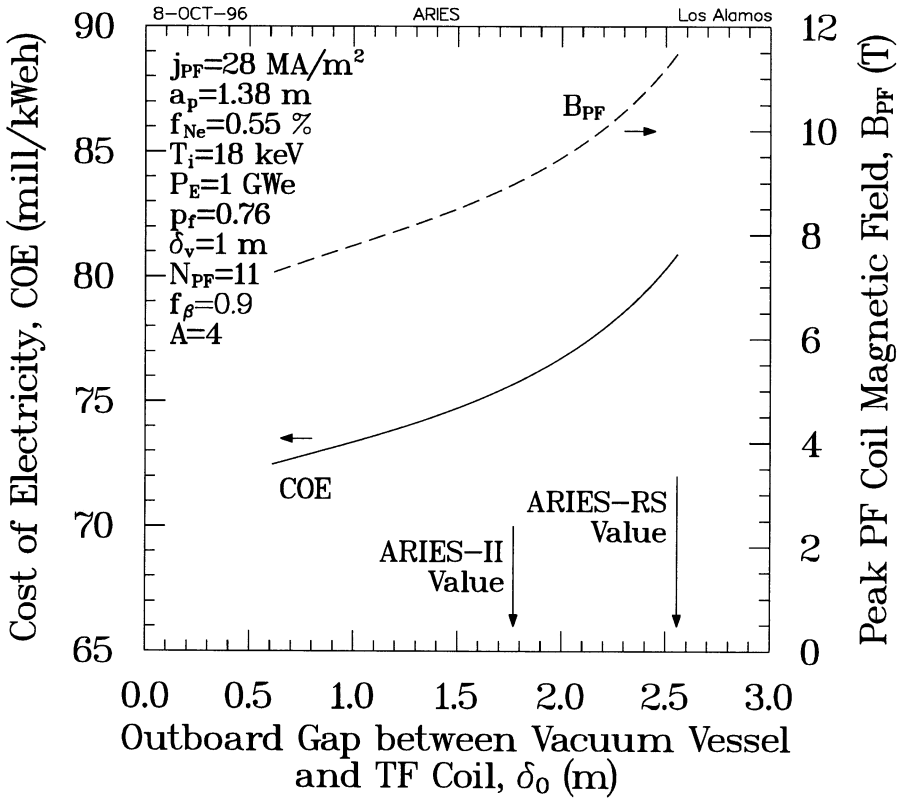

Fig. 25. COE (left scale) and the peak field at the PF-coils (right scale) as a function of the gap thickness between the vacuum vessel and the TF-coil (Fig. 24) for the fixed parameters of Table 4.

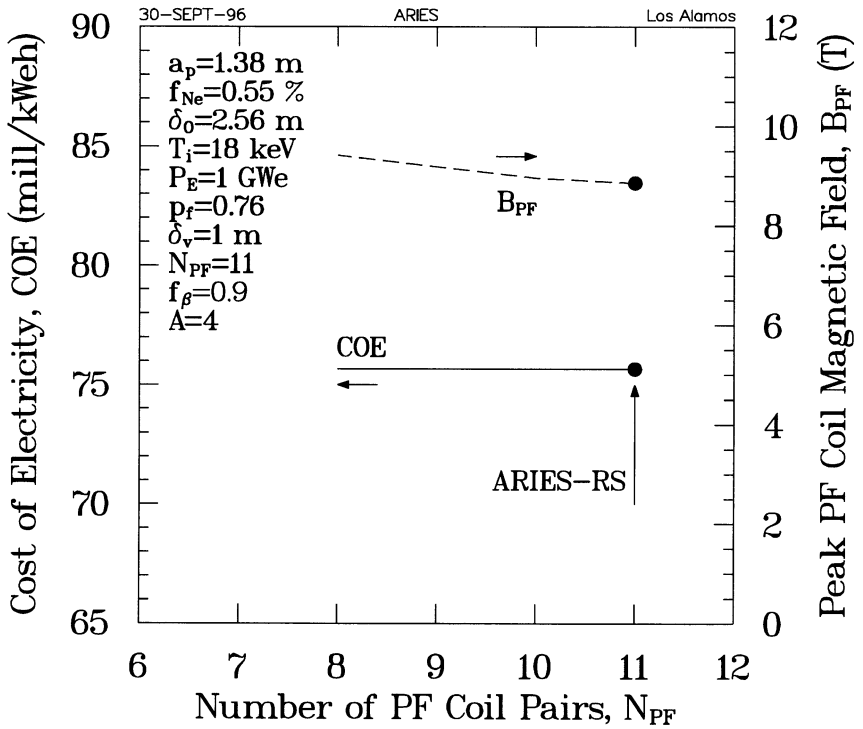

Fig. 26. The cost of electricity (left scale) and the peak field at the PF-coils (right scale) as a function of the number of PF-coils for the fixed parameters of Table 4.

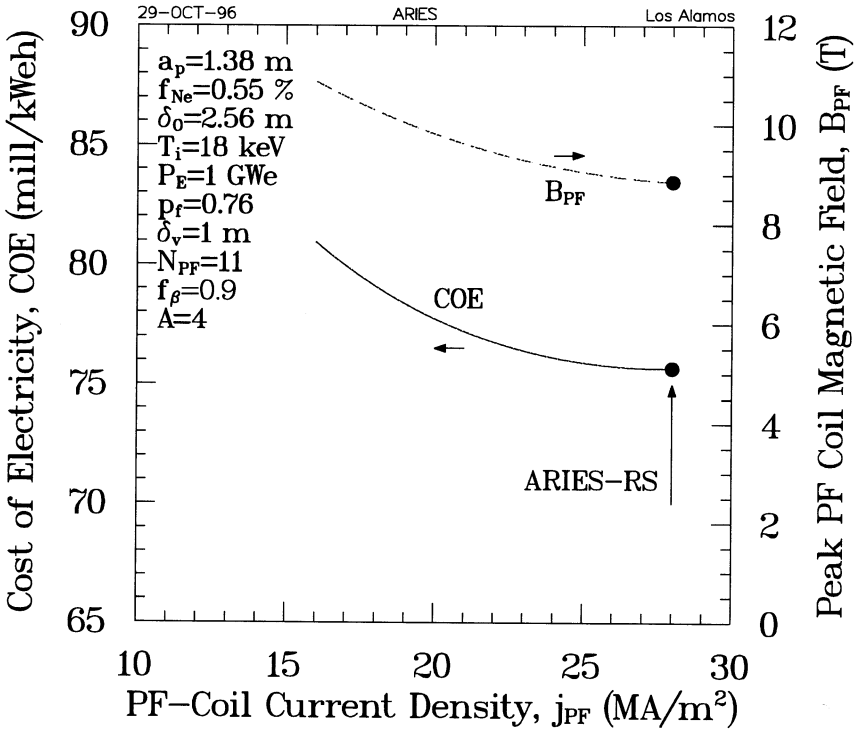

Fig. 27. The cost of electricity (left scale) and the peak field at the PF-coils (right scale) as a function of the PF-coil current density for the fixed parameters of Table 4.

increase of approximately 6 mill kW_eh^{-1} relative to the cost of electricity reported in Ref. [1] for a reverse-shear design. The inclusion of a non-zero edge density not only increased the cost of electricity, but perturbed the cost-minimizing plasma temperature to a higher value (from 14 to 18 keV).

Two issues remain unresolved for the ARIES-RS design: determination of the optimum aspect ratio and compliance with a peak-field constraint for the PF-coils and the consequences of exceeding that constraint. To accurately determine the optimum aspect ratio requires more detailed quantification of the liabilities associated with decreasing aspect ratio (e.g. the cost penalties expected for increased engineering design difficulties at lower aspect ratio) than was done herein. For the PF-coil peak-field constraint, the field at which the superconductor must be switched from NbTi to Nb_3Sn and the cost differential between the two superconductors must be known before the cost-minimized methods complying with this constraint can be determined. However, a few compliance methods have been suggested that incur only an ≈ 0.5 mill kW_eh^{-1} cost penalty (e.g. increasing the minor radius to 1.45 m).

Systems analysis has been used to minimize the cost of electricity with respect to the plasma minor radius and the temperature. A design without these optimizations could suffer significant cost penalties (e.g. arbitrarily choosing a plasma tem-

Table 5
Reference unit costs

Commodity	1992 $
Magnets ($ kg^{-1})	
PF-coils	81.7
TF-coils	92.7
Current-drive system ($ W^{-1})	1.3
Vanadium ($ kg^{-1})	300
Structural steel ($ kg^{-1})	67.7

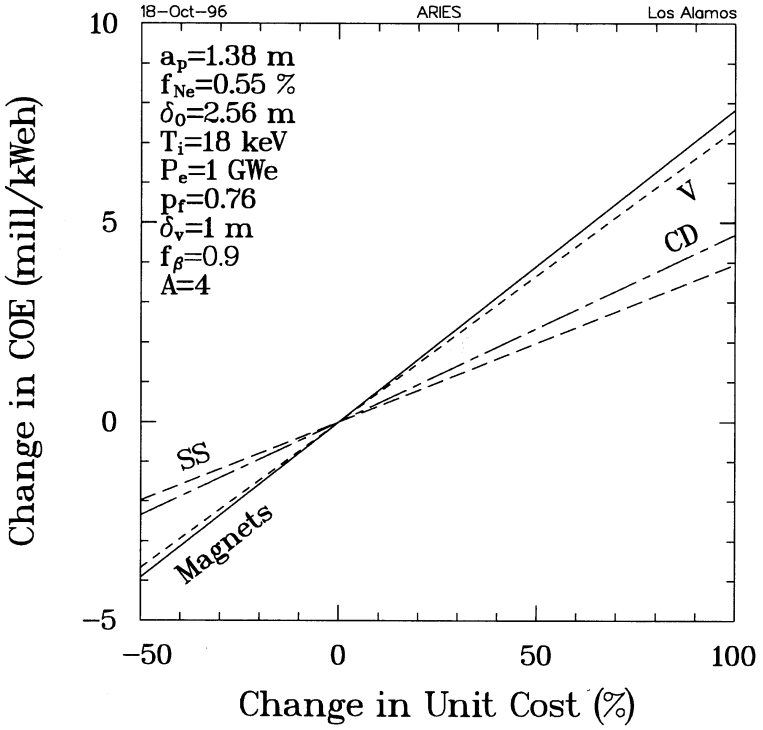

Fig. 28. The incremental change in the cost of electricity for reverse shear parameters as a function of the change in the unit cost for the magnets, the current-drive system (CD), vanadium (V), and structural-grade steel (SS) for the fixed economic parameters of Table 5.

perature of 10 keV would increase the cost of electricity from 76 mill kW_eh^{-1} for the optimized reference design to 95 mill kW_eh^{-1}). Systems analysis has also been used to demonstrate that adding impurities to the plasma core does not ameliorate the divertor problem, as was first expected. The sensitivity of the cost of electricity to unit costs indicates the greatest sensitivity is in the unit costs of the magnets and vanadium and that a doubling of either would increase the cost of electricity by only $\leq 12\%$.

References

[1] F. Najmabadi et al., The Starlite Project assessment phase report, University of California San Diego Report UCSD-ENG-005, 1997.

[2] F. Najmabadi, R.W. Conn, et al., The ARIES-II and -IV second stability tokamak reactors, University of California Los Angeles Report UCLA-PPG-1461 (to be published); also F. Najmabadi, R.W. Conn, et al., Directions for Attractive Tokamak Reactors: The ARIES-II and ARIES-IV Second-Stability Designs, Proc. 14th Int. Conf. Plasma Phys. and Controlled Nucl. Fus. Res., Würzburg, Germany (October 1992), International Atomic Energy Agency, Vienna (1993) 295.

[3] F. Najmabadi, et al., The PULSAR tokamak reactor study, University of California San Diego Report UCSD-ENG-003, 1997.

[4] M.S. Tillack, S. Malang, L. Waganer, et al., Configuration and engineering design of the ARIES-RS tokamak power plant, Fus. Eng. Des. 38 (1997) 87–113.

[5] L.A. El-Guebaly, The ARIES Team, Overview of ARIES-RS neutronics and radiation shielding: key issues and main conclusions, Fus. Eng. Des. 38 (1997) 139–158.

[6] F. Najmabadi, et al., The ARIES-RS tokamak power plant: final design report, University of California San Diego Report UCSD-ENG-007, 1997.

[7] D.E. Post, K. Borrass, J.D. Callen, et al., ITER physics, Int. Thermonucl. Exp. Reactor Documentation Ser. No. 21 (November 1990).

[8] F. Najmabadi, R.W. Conn, The ARIES-I tokamak reactor study, University of California Los Angles Report UCLA-PPG-1323, 1991.

[9] F. Najmabadi, R.W. Conn, The ARIES-III D-^{3}He tokamak reactor study, University of California Los Angles Report UCLA-PPG-1384, 1992.
[10] S.C. Jardin, C.E. Kessel, C.G. Bathke, et al., Physics basis for a reversed shear tokamak power plant, Fus. Eng. Des. 38 (1997) 27–57.
[11] F. Najmabadi, M.S. Tillack, The ARIES Team, Overview of the ARIES-RS reversed shear power plant study, Fus. Eng. Des. 38 (1997) 3–25.
[12] L. Bromberg, P. Titus, J. Schultz, M. Sidorov, The ARIES Team, ARIES-RS magnet systems, Fus. Eng. Des. 38 (1997) 159–188.